Mechanics in Nano-Engineering 1(1) (2027) 58-82

Ministry of Science, Research and Technology
University of Bonab

Mechanics in Nano-Engineering

journal homepage: https://mneng.ubonab.ac.ir/

Mechanics in NANO-ENGINEERING

Dynamic Simulation of Nanoscale Particle Motion Driven by Atomic Force Microscope Probe in Nanomanipulation Applications

Leila Mohammadian [a,*], Asghar Mohammadian [b]

[a] Department of Electrical Engineering, Shab.C., Islamic Azad University, Shabestar, Iran

[b]Department of Electrical Engineering, Ilk.C., Islamic Azad University, Ilkhchi, Iran

ARTICLE INFO

Article history:
Received 6 14 2026
Received in revised form 8 25 2026
Accepted 10 27 2026

Keywords:
Atomic Force Microscopy (AFM);
Nanomanipulation;
JKR Model;
Adhesion Forces;
Newton's Second Law;
Scanning Probe Microscopy (SPM)

ABSTRACT

The Atomic Force Microscope (AFM) is a versatile nanorobotic platform for imaging and controlled manipulation of nanoscale objects. This paper presents a dynamic simulation of a spherical gold nanoparticle pushed by an AFM probe on a silicon oxide substrate. Contact deformation and adhesion are governed by the Johnson-Kendall-Roberts (JKR) model, while friction follows a modified Coulomb law with an interfacial shear strength of 28 MPa. A two-phase algorithm captures the manipulation process. During the sticking phase, the lateral cantilever force increases until reaching the sliding or rolling threshold. In the slipping phase, transient particle motion is solved by integrating Newton's second law using an adaptive Runge-Kutta integrator, modeling the cantilever as a linear spring. Although the particle's inertial time scale is negligible compared to the pushing time, leading to quasi-static mean motion, the full dynamic solution captures nanoscale stick-slip cycles. The lateral force oscillates between the static friction threshold and a lower kinetic boundary governed by a kinetic-to-static friction ratio of 0.89, producing approximately 50-nanometer slip events lasting under a microsecond. For the baseline case, sliding initiates at 0.213 seconds with a critical force of 0.647 micro-Newtons, preceding rolling by 0.107 seconds. Across examined material configurations, sliding consistently precedes rolling, with the rolling-to-sliding force ratio ranging from 1.24 to 1.37. Validated against analytical solutions, these parametric findings regarding particle radius, tip radius, and contact angle provide robust guidelines for optimizing AFM nanomanipulation protocols.

1. Introduction

The ability to position, move, and assemble individual atoms and molecules has been a central aspiration of nanotechnology since Feynman's visionary 1959 lecture, 'There's Plenty of Room at the Bottom.' The realization of this vision became tangible with the invention of the Scanning Tunneling Microscope (STM) by Binnig and Rohrer in 1981 [1], for which they received the Nobel

* Corresponding author.
E-mail addresses: Le.mohammadian@iau.ac.ir , Asghar.mohammadian@iau.ac.ir
http://dx.doi.org
© 2027 Published by University of Bonab

Prize in Physics in 1986. The STM's capability to image and locally probes conductive surfaces with sub-atomic resolution represented a paradigm shift in surface science. Building upon this foundation, Binnig, Quate, and Gerber introduced the Atomic Force Microscope (AFM) in 1986 [2], extending high-resolution probe microscopy to non-conductive materials, biological specimens, and ambient environments.

The most dramatic early demonstration of atomic-scale manipulation came in 1990, when Eigler and Schweizer [3] used a low-temperature STM to spell out 'IBM' by repositioning 35 individual xenon atoms on a nickel surface with atomic precision. This landmark experiment validated the conceptual framework for bottom-up nanotechnology and catalyzed worldwide interest in probe-based nanomanipulation. Subsequent advances established a broad toolkit of SPM-based manipulation strategies, including lateral pushing, vertical pick-and-place, field-induced atom transfer, and chemical bond formation [4-5].

In the context of nanorobotics, the AFM is regarded as a paradigmatic nanorobotic platform: its cantilever acts as an elastic arm, its probe tip as an end-effector, and its piezoelectric scanner as a positioning stage — providing up to six degrees of freedom in force-controlled interaction with nanoscale specimens [6-7]. AFM-based nanomanipulation of nanoparticles — including gold nanoclusters, semiconductor quantum dots, carbon nanotubes, and biological entities — has been demonstrated in numerous studies [8–15]. The ability to reliably control nanoparticle position, orientation, and trajectory is foundational for nano-assembly, single-molecule force spectroscopy, nano-device fabrication, and targeted biological manipulation.

Despite its widespread use, AFM nanomanipulation remains a technically demanding and low-throughput process. A critical bottleneck is the limited availability of quantitative predictive models that relate experimentally controllable parameters — probe geometry, material properties, substrate velocity, applied force — to the resulting particle dynamics. Early experimental studies [8-9] established qualitative descriptions of pushing mechanics; however, systematic dynamic models capable of predicting critical forces, onset times, and motion modes (sliding, rolling, spinning) as functions of all relevant parameters are still an active area of research.

Sitti and Hashimoto [8] pioneered the quantitative modeling of controlled nanoparticle pushing using AFM, introducing the concept of critical force thresholds for motion onset and providing experimental validation with gold nanoparticles on silicon. Subsequent works, [10–14] significantly extended this framework to incorporate three-dimensional dynamics, cylindrical particle geometries, LuGre friction models, rough-surface contact mechanics, and biological particle manipulation. Parallel efforts have addressed the role of environmental conditions (liquid vs. air), capillary forces, electrostatic interactions, and substrate heterogeneity on manipulation outcomes [15–20].

This paper contributes to this body of work in three ways. First, the post-onset (Phase II) motion is obtained by integrating Newton's second law for the particle–cantilever system instead of prescribing a constant force, so that inertia, the drop from static to kinetic friction, and the cantilever compliance are retained. Second, the numerical method is stated explicitly and verified against an analytical solution. Third, a parametric study with respect to particle radius, probe tip radius, initial contact angle and material moduli quantifies how robust the sliding-before-rolling ordering is, and the dynamic solution predicts a stick–slip cycle that can be tested experimentally. The model uses JKR contact mechanics and a modified Coulomb friction law.

2. Literature Review

2.1 Foundations of Scanning Probe Microscopy and Atomic Manipulation

Scanning probe manipulation began with the STM [1,4], which Eigler and Schweizer used to position single xenon atoms on Ni(110) at 4 K [3] and Crommie et al. used to build quantum corrals [5]. The AFM extended force-based imaging and manipulation to insulating samples and ambient conditions [2].

2.2 AFM as a Nanorobotic Platform

The AFM cantilever–tip–scanner assembly is commonly viewed as a nanorobotic arm with an end-effector and a positioning stage [6-7]. Nanorobotic systems that combine probes with scanning electron microscopes have been used to bend, cut and reposition carbon nanotubes [6,7,24], and automated AFM manipulation relies on image feedback to cope with thermal drift and tip wear [15].

2.3 Contact Mechanics at the Nanoscale: JKR and Related Models

The accurate modeling of tip–particle–substrate contact forces is essential for quantitative nanomanipulation simulation. At the nanoscale, adhesion forces — including van der Waals, capillary, and electrostatic contributions — become dominant over gravitational and inertial forces, requiring contact mechanics frameworks that explicitly account for surface energy.

The Johnson–Kendall–Roberts (JKR) model [16], originally developed in 1971 for elastic spheres in adhesive contact, remains the most widely used framework for AFM nanomanipulation modeling. The JKR model predicts a finite contact area and pull-off force even at zero applied load, consistent with experimental observations for compliant, high-surface-energy contacts. The competing Derjaguin–Muller–Toporov (DMT) model [17] applies to stiffer, lower-energy contacts with longer-range adhesion and predicts a different pull-off force and contact area evolution.

For intermediate cases, the Maugis–Dugdale transition parameter determines which model is appropriate. Korayem and Taheri [11] systematically compared JKR, DMT, BCP (Bradley–Muller–Tuck), COS, PT, and SUN contact models for biological micro/nanoparticle manipulation, finding that model selection significantly affects predicted critical forces and contact areas. For gold nanoparticles on silicon — the system studied in the present work — the JKR model has been validated experimentally and is the model of choice in the literature [8,10-11].

2.4 Dynamic Modeling of Nanoparticle Pushing

In [8] the first quantitative model of controlled nanoparticle pushing with an AFM was presented. It distinguishes sliding from rolling and shows that, at the nanoscale, sliding precedes rolling because of adhesion; the model uses JKR contact mechanics and Coulomb friction and was compared with experiments on gold nanoparticles. A dynamic simulation of nanoparticle sliding during probe-based positioning was given in [26].

In [10], this framework was extended to a full 2D sensitivity analysis of AFM-based nanomanipulation, systematically investigating the dependence of critical pushing force and time on all model parameters — including particle radius, tip radius, surface energy, friction coefficients, and material moduli — for gold nanoparticles on silicon substrates. Their results provided the first comprehensive parametric map of nanomanipulation critical conditions, enabling systematic optimization of experimental protocols.

In [12-13], further developed 3D dynamic models for nanoparticle manipulation, extending the lumped-parameter approach to include full spatial dynamics, cantilever torsion, and three-dimensional force decomposition. These models enabled the prediction of manipulation trajectories for complex substrate geometries and multi-step assembly sequences.

An important extension was provided by the introduction of the LuGre friction model in place of the classical Coulomb model [13-14]. The LuGre model captures pre-slip displacement, friction delay, and stick-slip behavior — phenomena that are experimentally observed in nanoscale tribology but absent from simpler friction laws. [14] demonstrated that inclusion of LuGre friction significantly improves the accuracy of predicted nanoparticle trajectories, particularly in the transition region between sticking and sliding.

For non-spherical nanoparticles, [12] developed a dynamic model for cylindrical particle pushing (applicable to carbon nanotubes and nanowires), incorporating distributed friction forces along the contact length and kinematic relations for determination of the instantaneous pushing-point position. Simulations for MWCNTs with different diameters and lengths revealed rich dynamic behavior, including spinning and rolling transitions not present in the spherical-particle model.

2.5 Advanced AFM Platforms and High-Speed Imaging

Conventional AFM instruments are limited to imaging speeds of the order of one frame per minute, which precludes observation of dynamic biological and chemical processes. The development of high-speed AFM (HS-AFM) [18] achieved video-rate imaging (10–30 frames/s) of biological macromolecules, enabling real-time observation of motor protein dynamics, DNA conformational changes, and membrane protein interactions at the molecular scale.

The FIRAT (Force-sensing Integrated Readout and Active Tip) platform [20], developed at the Georgia Institute of Technology, achieves imaging speeds approximately 100 times faster than conventional AFM while simultaneously measuring multiple surface properties — topography, adhesion energy, contact time, and surface stiffness — in a single contact event. The FIRAT probe, smaller than the tip of a standard sewing needle, is fabricated using MEMS technology and integrates a piezoresistive force sensor with an active tip actuator, enabling both high-speed imaging and multi-property mapping.

2.6 Nanomanipulation of Biological and Functional Nanoparticles

The application of AFM nanomanipulation to biological systems has emerged as a major research direction. [11] modeled the biomanipulation of DNA strands, yeast cells, platelets, and nanobacteria using various contact mechanics models, demonstrating that the choice of contact model critically affects predicted manipulation outcomes for soft biological particles. The viscoelastic nature of biological particles — which exhibit time-dependent deformation and energy dissipation during contact — necessitates contact models beyond the elastic JKR framework.

In [19], rough viscoelastic contact models were developed for the first phase of 3D biological particle manipulation, incorporating surface topography and material viscoelasticity into the pre-motion adhesion analysis. Their results demonstrated that surface roughness can significantly reduce the effective adhesion and hence the critical pushing force, with implications for the manipulation of particles on heterogeneous biological substrates.

In [21], imaging and manipulation of polystyrene nanoparticles using AFM is developed, extending the framework from spherical to anisotropic particle geometries and showing that nanorod orientation strongly influences the critical force and trajectory during pushing. In [22], the sliding and rolling tribological behavior of individual ZnO nanowires under AFM manipulation, providing experimental validation of the dynamic transition between motion modes and quantifying the anisotropic friction of one-dimensional nanomaterials, is studied.

2.7 Automated and Controlled Nanomanipulation

Achieving reliable, repeatable nanomanipulation requires not only accurate dynamic models but also robust control strategies. [14] applied sliding mode control (SMC) to AFM-based nanomanipulation, providing trajectory tracking in the presence of piezoelectric hysteresis, thermal drift, and model uncertainties. SMC's robustness to matched disturbances makes it well-suited to the highly nonlinear, uncertain dynamics of nanoscale pushing.

Automated nanomanipulation — eliminating the need for continuous human intervention through real-time image analysis and model-predictive control — has been demonstrated for both spherical nanoparticles [15] and carbon nanotubes [6]. These systems integrate AFM imaging with manipulation in a closed-loop cycle: image acquisition, target identification, trajectory planning, manipulation execution, and verification imaging. Achieving full automation requires robust solutions to tip-particle registration, manipulation outcome prediction, and error recovery — challenges that remain active areas of investigation.

3. Theoretical Framework

3.1 Interatomic Forces and Potentials

The physical origin of all material cohesion and tribological behavior at the nanoscale lies in interatomic interaction forces. In molecular dynamics (MD) and quasi-static contact mechanics approaches, these forces are derived from empirical potential energy functions. The principal potentials employed in nanoscale modeling are summarized in Table 1.

Table 1. Principal interatomic interaction potentials used in nanoscale simulation and their physical significance.

Force / Potential	Mathematical Expression and Physical Significance
Harmonic Spring (Bond Stretching)	$V = K(r - r_0)^2$ [K: bond stiffness; r_0: equilibrium bond length; models covalent bonds and contact springs]
Coulombic (Electrostatic)	$V = q_i q_j / (4\pi\varepsilon_0 r_{ij})$ [q_i,q_j: ionic charges; ε_0: vacuum permittivity; r_{ij}: separation; governs tip–substrate electrostatics]
Lennard-Jones (van der Waals)	$V(r_{ij}) = 4\varepsilon_{ij}[(\sigma_{ij}/r_{ij})^{12} - (\sigma_{ij}/r_{ij})^6]$ [σ_{ij}: collision diameter; ε_{ij}: well depth; dominant at short range in tip–particle adhesion]
Total Molecular Energy	$E_{total} = \Sigma V_{bond} + \Sigma V_{angle} + \Sigma V_{torsion} + \Sigma V_{nonbonded}$ [sum of all bonded and non-bonded interaction contributions]

3.2 Simulation Parameters and Notation

Table 2. Notation, physical meaning and values of the parameters used in the simulation.

Symbol	Physical Meaning	Value / Units
K	Effective spring constant of the virtual interatomic bond (harmonic potential)	*N/m*
σ_{ij}	Lennard-Jones collision diameter for atom pair i–j	*Å*
ε_{ij}	Lennard-Jones well depth for atom pair i–j	*J*
q_i	Ionic charge of the i-th atom in the electrostatic interaction	*[e]*
x	Instantaneous position of the oscillating atom	*nm*
x_o	Equilibrium position of the oscillating atom	*nm*
r_{ij}	Interatomic separation between atoms i and j	*nm*
ε_o	Permittivity of vacuum	8.854×10^{-12} *C²/(N·m²)*
R_p	Radius of the spherical gold nanoparticle	500 nm
R_{tip}	Radius of the AFM probe tip apex (spherical approximation)	30 nm
ρ	Density of gold	*19 300 kg/m³*
m	Particle mass, $m = 4\pi\rho R_p^3/3$	$1.01\times10-14$ kg
V_{sub}	Constant velocity of the moving silicon oxide substrate	*1 μm/s*
k_c	Effective lateral cantilever stiffness (lateral loading rate $k_c V_{sub}$ = 2.0 μN/s)	*2.0 N/m*
K_{eff}	Effective elastic modulus in the JKR contact model	*54.8 GPa* (5.48×10^{10} *Pa*)
E, G, ν	Young's modulus, shear modulus and Poisson's ratio; $G = E/[2(1+\nu)]$	*Cases A–C in Table 3;* $\nu = 0.270$
γ	Work of adhesion per unit area at the particle–substrate interface	*21.4 mJ/m²* (a_{sp} *= 20.3 nm)*
μ_s	Static friction coefficient at the particle–substrate interface	*0.8*
μ_d	Kinetic friction coefficient at the particle–substrate interface	*0.7*
τ	Interfacial shear strength (area-independent); friction force = τA	*28 MPa*
ζ	Ratio of kinetic to static friction force, F_d/F_s (Eq. 6)	*0.886*
F^*	Critical force (resultant tip force) at sliding onset	*0.647 μN*
F_s	Lateral critical force at onset (static friction force), F_Y^*	*0.426 μN*
F_Z	Normal component of the tip force (pre-load), constant in Phase I	*0.487 μN*
F_T	Resultant tip-to-particle force applied by the cantilever, $F_T = (F_Y^2+F_Z^2)^{1/2}$	*μN*
κ	Rolling-resistance coefficient, $M_r = \kappa\tau A_{sp} R_p$	*14.8*
θ_{tip}	Angle of the probe force vector relative to the substrate horizontal	*rad*
α	Contact angle of the tip on the particle, measured from the vertical	*1.05 rad (60°)*

3.3 Governing Equations of Motion

Following specification of the interatomic force model, the time evolution of particle position and velocity is obtained by numerical integration of Newton's second law (applied to the slipping phase in Section 4.4.2). For a particle of mass *m* moving in three-dimensional space: Although the

translational motion is fully solved using Newton's second law, the rotational inertia (I_θ) is neglected since the primary predicted motion mode is pure sliding.

$$\vec{F} = m \cdot \vec{a} = m \cdot \left(d^2\vec{r}/dt^2\right) \quad \textbf{(1)}$$

where $\vec{F}$ is the resultant force vector, and $\vec{r}$ is the position vector. At each time step Δt, particle positions and velocities are updated from the computed force field. The relationship between force and potential energy in three dimensions is given by the gradient operator:

$$\vec{F} = -\nabla V = -\left(\hat{\imath}\partial V/\partial x + \hat{\jmath}\partial V/\partial y + \hat{k}\partial V/\partial z\right) \quad \textbf{(2)}$$

In one-dimensional form, this reduces to $F = -dV/dr$, from which all interatomic force expressions in Table 1 are derived by differentiation of the corresponding potential function with respect to the interatomic separation.

4. Dynamic Model of Nanoparticle Motion During AFM Pushing

4.1 System Configuration and Assumptions

The simulation models an AFM cantilever with a cylindrical beam cross-section and a spherical apex of radius R_{tip}, interacting with a rigid spherical gold nanoparticle (radius R_p) on a planar silicon oxide substrate moving at constant velocity V_{sub}. Figure 1 illustrates the system geometry and the relevant geometric and force parameters.

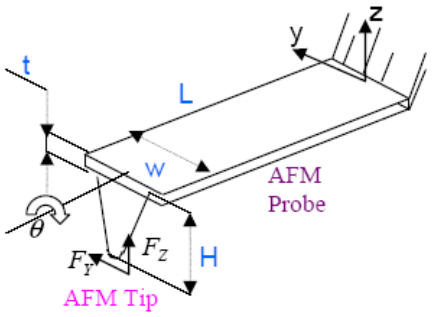


Figure 1. Schematic of the AFM nanomanipulation system: cantilever probe (length L, width w, thickness t, tip height H), spherical gold nanoparticle and silicon oxide substrate.

An initial lateral pre-displacement δ_0 is imposed on the cantilever about the y-axis before substrate motion to guarantee positive probe–particle contact throughout Phase I. The following simplifying assumptions are adopted:

- The nanoparticle is modeled as a rigid sphere; elastic deformation is confined to the tip–particle and particle–substrate contact zones, described by the JKR model.
- No external forces act along the x-axis before manipulation; all driving forces originate from the cantilever probe.

- The substrate moves at constant velocity V_{sub} along the x-axis; any lateral drift is neglected.
- Friction at both contact interfaces (tip–particle and particle–substrate) is described by a modified Coulomb law with a load-dependent and an area-dependent term, $F = \mu N + \tau A$ (Section 4.3).
- The cantilever acts on the particle through a linear lateral spring of stiffness k_c; the normal force at the particle–substrate interface is constant during Phase II (its variation during Phase I is below 0.5 % and is neglected).
- The translational inertia of the particle is retained in Phase II. Rotation is not integrated, because the rolling threshold is not reached before, or during, sliding (Section 6.2).

4.2 Probe and Cantilever Dynamics — Free Body Diagram

Figure 2 shows the free body diagram of the AFM probe tip and the corresponding angular displacement and linear motion of the cantilever during particle pushing. The force F_T exerted by the cantilever tip on the nanoparticle acts along the probe axis at angle θ_{tip} relative to the substrate. The contact angle α between the probe tip apex and the particle surface determines the decomposition of F_T into normal and tangential components.

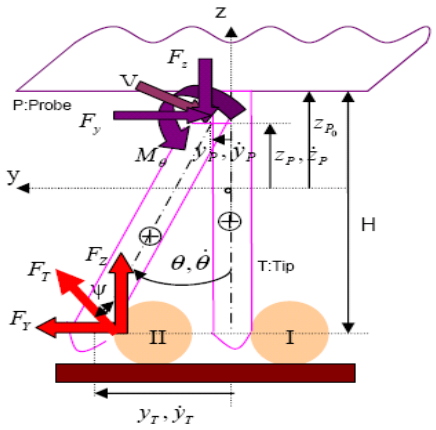


Figure 2. Free body diagram of the AFM probe tip apex during nanoparticle pushing.

4.3 Force Model: Normal and Frictional Forces During Particle Pushing

Figure 3 shows the full force diagram for the nanoparticle during lateral pushing, including contributions from the AFM tip and the substrate. The normal force at the particle–substrate interface and the lateral cantilever force collectively determine the onset of particle motion.

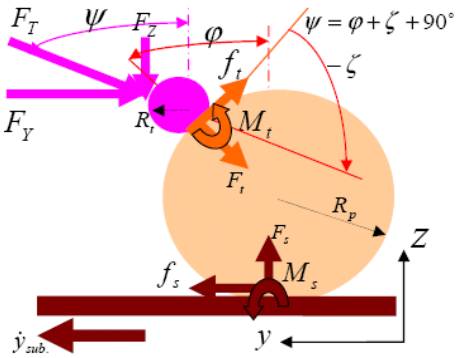


Figure 3. Force and dynamics diagram of the spherical nanoparticle during AFM-driven displacement.

As the substrate moves at constant velocity V_{sub}, the lateral cantilever force F_Y grows (Phase I). The critical conditions for sliding and rolling follow from the force balance of Fig. 3, with the contact radii given by the JKR model and the friction forces by the modified Coulomb law below [8,10]. Motion starts when F_T first reaches the lower of the two thresholds, which, as shown in Section 6.2, is the sliding threshold.

The JKR contact radius a of an interface with effective radius R, effective modulus K_{eff}, work of adhesion γ and normal load N is:

$$a^3 = (R/K_{eff})\left[N + 3\pi\gamma R + \sqrt{(6\pi\gamma RN + (3\pi\gamma R)^2)}\right], A = \pi a^2 \quad \textbf{(3)}$$

with $R = R_p$ for the particle–substrate interface and $R = R_pR_{tip}/(R_p+R_{tip})$ for the tip–particle interface. The friction force at an interface is the sum of a load-dependent and an area-dependent term:

$$F_s = \mu_s N + \tau A_{sp} \quad \textit{(static; defines the sliding threshold } F_Y{}^* = F_s) \quad \textbf{(4)}$$

$$F_d = \mu_d N + \tau A_{sp} \qquad \textit{(kinetic)} \quad \textbf{(5)}$$

Here τ is the interfacial shear strength in Pa (28 MPa, independent of area) [22-23] and $A_{sp} = \pi a_{sp}^2$ is the particle–substrate contact area, so μN and τA are both forces in N. The "shear strength parameter" τ_s in Pa·m listed in the previous version belongs to line-contact (cylindrical) formulations, in which friction is expressed per unit contact length [12-13]. The ratio of kinetic to static friction force,

$$\zeta = F_d/F_s \; ; \; F_T(t) = \sqrt{\left(F_Z{}^2 + F_Y{}^2\right)}, \psi(t) = arctan(F_Y/F_Z);$$
$$F^*s(t) = \tau A_{sp}/(sin\psi - \mu_s cos\psi) \quad \textbf{(6)}$$
$$F^*s(t) = \tau A_{sp}/(sin\psi - \mu_s cos\psi)$$

controls the force drop at the onset of sliding. For the baseline case (F_s = 0.426 μN, N = F_Z = 0.487 μN, μ_s = 0.8, μ_d = 0.7), Eq. (4) gives $\tau A_{sp} = F_s - \mu_s N$ = 36 nN, which corresponds to a_{sp} = 20.3 nm; Eq. (5) gives F_d = 0.377 μN and Eq. (6) gives ζ = 0.886. Friction is load-dominated ($\mu_s N$ is 91 % of F_s), and $\zeta \to \mu_d/\mu_s$ = 0.875 as $\tau A_{sp} \to 0$.

The cantilever force on the particle has a lateral component that grows linearly with time, $F_Y = k_c V_{sub} t$, and a normal component F_Z fixed by the pre-displacement δ_0. The resultant and its inclination to the vertical are $F_T(t), \psi(t)$.

Sliding starts when $F_Y = F_T \sin\psi$ reaches F_s of Eq. (4) with $N = F_Z = F_T \cos\psi$. This gives the critical resultant force $F^*_s(t)$.

where A_{sp} is evaluated from Eq. (3) with $N = F_Z$. The denominator vanishes at $\tan\psi = \mu_s$, i.e. at $t = \mu_s F_Z/(k_c V_{sub})$; before that time F^*_s is negative and has no physical meaning. The sliding onset t^* follows from $F_T(t^*) = F^*_s(t^*)$, or equivalently $k_c V_{sub} t^* = \mu_s F_Z + \tau A_{sp}$. Rolling about the particle–substrate contact point starts when the moment of the tip force about that point, applied at the contact angle α from the vertical, exceeds the rolling-resistance moment $M_r = \kappa \tau A_{sp} R_p$:

In $F_r^*(t)$ κ is a dimensionless rolling-resistance coefficient, and F^*_r has its pole at $\tan\psi = \tan(\alpha/2)$. Eq.(6) for $F^*_s(t)$, contains no tip geometry, so the sliding threshold does not depend on R_{tip} or α, while the rolling threshold does (Section 6.7). In this study α = 60° and κ = 14.8, where κ was calibrated to the rolling onsets of the three cases of Section 6.3–6.4; the rolling results are therefore consistency checks rather than independent predictions.

4.4 Two-Phase Simulation Algorithm

The simulation algorithm is organized into two sequential phases, as illustrated in Figure 4.

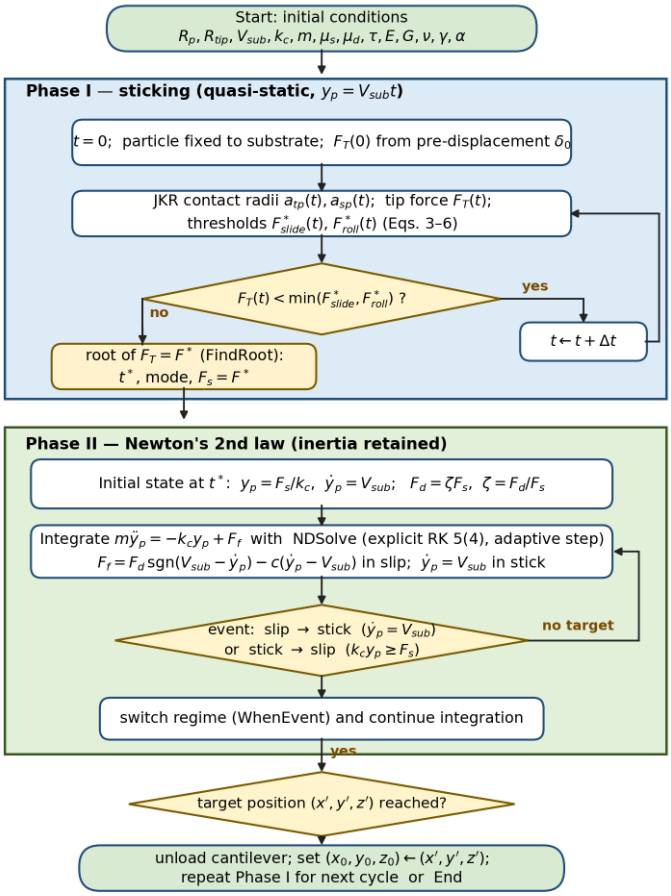


Figure 4. Two-phase simulation algorithm. Phase I (sticking) gives the onset time t* and the critical force $F_s = F^*$; *Phase II (slipping) integrates Newton's second law for the particle, with event detection for the stick–slip transitions.*

4.4.1 Phase I — Sticking phase

Phase I covers the interval [0, t*] during which the nanoparticle is carried with the substrate, $y_p = V_{sub}t$, so that its displacement relative to the substrate vanishes. The lateral cantilever force rises linearly, $F_Y = k_c V_{sub} t$, while the resultant force F_T also contains the normal pre-load produced by the pre-displacement δ_0 (***Eq. (6)***-$F_T(t)$, Fig. 14):

$$\Delta y(t) = y_p(t) - V_{sub}t = 0 \qquad for\ \ 0 \leq t < t^* \tag{7}$$

The onset time t* is the first root of $F_T(t) = F^*(t)$ on the physically admissible branch ($F^* > 0$) of the threshold curves,

$$F_T(t^*) = min[F^*_{slide}(t^*), F^*_{roll}(t^*)] = F^* \tag{8}$$

and the corresponding state (t*, F*) is the initial condition of Phase II.

4.4.2 Phase II — Slipping phase

At t = t* the lateral force reaches F_s and the interface starts to slip. Phase II solves Newton's second law (***Eq. 1***) for the lateral coordinate y_p of the particle in the laboratory frame (tip fixed, substrate moving at V_{sub}):

$$m\ddot{y}_p = -kcy_p + F_f, \qquad F_f = F_d sgn\left(V_{sub} - \dot{y}_p\right) - c\left(\dot{y}_p - V_{sub}\right)(slip) \tag{9}$$

where m is the particle mass, k_c the lateral cantilever stiffness and c a viscous damping coefficient (c = 0 in the baseline case). The initial conditions are $y_p(t^*) = F_s/k_c$ and $\dot{y}_p(t^*) = V_{sub}$. The particle sticks to the substrate again when its velocity returns to V_{sub}, and slips again when the spring force reaches F_s:

$$\dot{y}_p = V_{sub} \qquad (stick,\ while\ k_c y_p < F_s);\ \ stick \rightarrow slip\ when\ k_c y_p = F_s \tag{10}$$

With $Y = k_c y_p/F_s$, $\eta = \omega t$, $\omega = \sqrt{(k_c/m)}$ and $\Theta = k_c V_{sub}/(F_s\omega)$, one slip event with c = 0 is governed by:

$$Y'' + Y = \zeta, \qquad Y(0) = 1, \qquad Y'(0) = \Theta \tag{11}$$

whose solution is

$$Y(\eta) = \zeta + (1-\zeta)cos\eta + \Theta sin\eta, \quad \eta_e = 2\left[\pi - arctan\left((1-\zeta)/\Theta\right)\right] \tag{12}$$

where η_e is the end of the slip ($Y' = \Theta$). Because $\Theta \ll 1 - \zeta$ ($\Theta = 3.3\times10^{-7}$ here), $\eta_e \approx \pi$ and

$$F_{min} \approx (2\zeta - 1)F_s, \quad t_{slip} \approx \pi\sqrt{(m/k_c)}, \qquad t_{stick} = (F_s - F_{min})/(k_c V_{sub}) \tag{13}$$

The displacement of the particle relative to the substrate is

$$\Delta y(t) = y_p(t) - V_{sub}t \tag{14}$$

In order to represent the stick–slip cycle the equation of motion is used.

Upon reaching the target position (x′, y′, z′), all cantilever forces are returned to zero, completing the manipulation cycle. For sequential operations the updated particle position (x′, y′, z′) replaces (x_0, y_0, z_0) as the initial condition of the next cycle.

5. Numerical Implementation

The model is implemented in Wolfram Mathematica in four modules: (i) general variables and parameters (Table 2), (ii) initial conditions, (iii) equations (JKR contact, force thresholds and the equation of motion) and (iv) plots. Phase I is a root-finding problem; Phase II is an initial-value problem integrated with NDSolve.

Phase I (onset). The thresholds $F^*_{slide}(t)$ and $F^*_{roll}(t)$ are algebraic functions of time through the JKR contact radii. They have a pole where their denominators vanish (Figs. 7 and 9–13), so t* is located with FindRoot from a bracketing interval on the admissible branch $F^* > 0$.

Phase II (time integration). Eq. (9) is integrated with NDSolve using an explicit Runge–Kutta pair of orders 5(4) (Dormand–Prince [34]). For $\dot{y} = f(t, y)$, each step of size h_n is

$$y_{n+1} = y_n + h_n \Sigma i = 17 b_i k_i, \qquad k_i = f\left(t_n + c_i h_n, y_n + h_n \Sigma j < i a_{ij} k_j\right) \tag{15}$$

The embedded fourth-order solution gives the error estimate e_n; a step is accepted if e_n is below the tolerance, and the next step is $h_{n+1} = h_n \min\{5, \max[0.2, 0.9\,(\mathrm{tol}/e_n)^{1/5}]\}$ [33].

Events. The stick-to-slip and slip-to-stick transitions (Eq. 10) are detected with WhenEvent, which locates the event inside the step and restarts the integration with the new regime. Treating the stick phase as the kinematic constraint $\dot{y}_p = V_{sub}$ is exact and avoids integrating about 10^7 oscillation periods per stick interval.

Settings. Equations are solved in the nondimensional form of Eq. (11) with Method → Explicit Runge Kutta (Difference Order 5), Accuracy Goal 12, Precision Goal 10 and Max Step Size 0.05 (in units of 1/ω). The script is provided as supplementary material, and the results were cross-checked with an independent explicit RK45 implementation (Section 6.8).

6. Results and Discussion

6.1 Contact Depth and Contact Area Evolution

As the tip force F_T increases with time, the tip–particle indentation grows, by a factor of about 2.3 over 0.5 s, while the particle–substrate indentation stays constant (Figure 5). Correspondingly the tip–particle contact radius grows from 10 nm to 15 nm, whereas the particle–substrate contact radius stays at 20.3 nm, with a change below 1 % (Figure 6). This follows from JKR theory: the tip contact responds to the growing resultant force F_T, whereas the substrate contact is governed by the normal load F_Z, which is constant in Phase I.

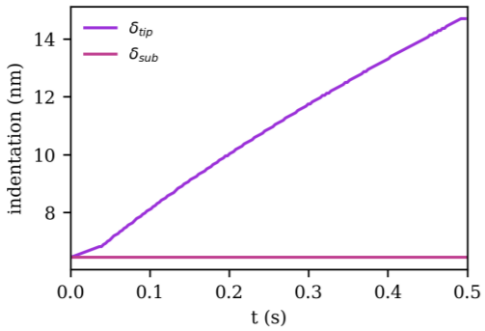


Figure 5. Evolution of the contact indentation with time at the tip–particle (δ_{tip}) and particle–substrate (δ_{sub}) interfaces, baseline conditions.

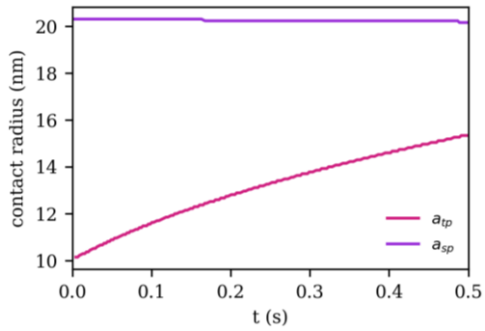


Figure 6. Evolution of the contact radii at the tip–particle (a_{tp}) and particle–substrate (a_{sp}) interfaces from the JKR model, baseline conditions.

6.2 Critical Force and Motion Onset: Sliding vs. Rolling

The transition from Phase I to Phase II occurs at the first intersection of the tip-force curve $F_T(t)$ with the critical-force curve $F^*_s(t)$ or $F^*_r(t)$ of ***Eqs. (6)***. Under the baseline conditions (Figures 7–9):

- Sliding onset: $t^* = 0.213$ s, $F^* = 0.647$ μN (lateral component $F_Y = 0.426$ μN) — first intersection; the motion mode is sliding.
- Rolling threshold: $t = 0.320$ s, $F_{roll} = 0.804$ μN — second intersection, reached 0.107 s after sliding has started.

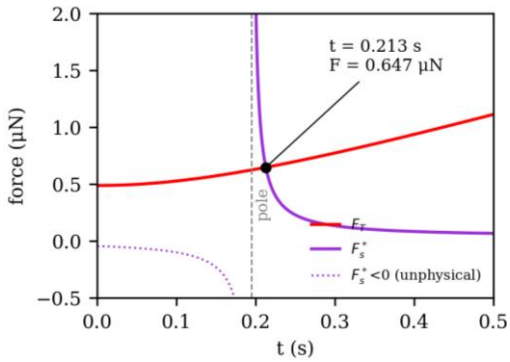


Figure 7. Tip force F_T and sliding critical force F^*_s (Eq. 6) versus time, baseline conditions. F^*_s has a pole at $t = \mu_s F_Z/(k_c V_{sub}) = 0.195$ s and is negative before it (dotted). The first intersection on the admissible branch, $t^* = 0.213$ s and $F^* = 0.647$ μN, marks the sliding onset.

The sliding-before-rolling ordering agrees qualitatively with [8]; the quantitative comparison is given in Section 6.8. At the nanoscale, adhesion makes the rolling resistance larger than the sliding resistance, F_{roll}/F_{slide} = 0.804/0.647 = 1.24 for the baseline case, whereas at the macroscale rolling friction is generally the lower of the two.

The present analysis adds (1) its quantification as the margin F_{roll}/F_{slide}, which is 1.24, 1.24 and 1.37 for cases A, B and C (Table 3), so the ordering holds in all cases studied; (2) the time margin between the two thresholds (0.107 s in the baseline case, 0.066 s in case B and 0.098 s in case C), which is the window in which a controller can stop the push before rolling can start; (3) the dependence of the margin on the controllable parameters (Section 6.7): the sliding threshold is independent of the tip radius and of the contact angle, whereas the rolling threshold increases with both, so the margin can be widened by tip positioning without changing the sliding force; and (4) the Phase II result (Section 6.5) that, during stick–slip, the lateral force never exceeds F_s, so the rolling threshold is not reached in steady pushing and the manipulation remains in the sliding mode.

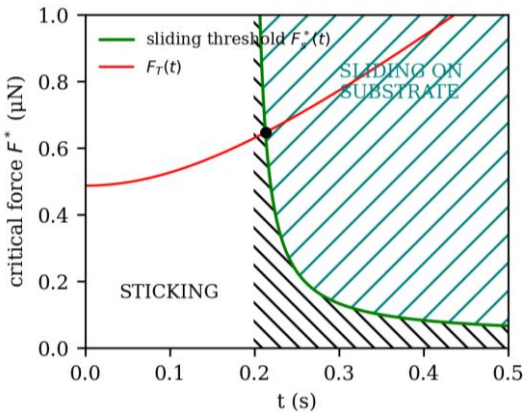


Figure 8. Map of the dynamic modes of the particle: sliding threshold $F^*_s(t)$ separating the sticking region (below) from sliding on the substrate (above), with the tip force $F_T(t)$. The first intersection, t^* = 0.213 s, marks the sliding onset.

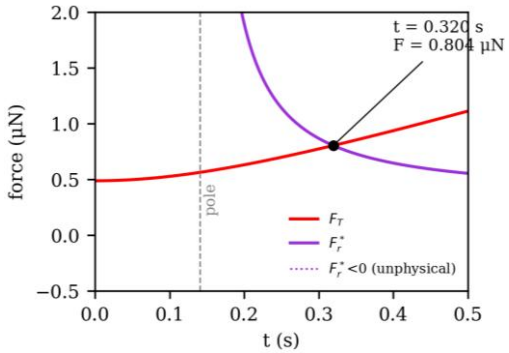


Figure 9. Tip force F_T and rolling critical force F^*_r (Eq. 6) versus time, baseline conditions (pole at 0.141 s): the second intersection at t = 0.320 s, F_{roll} = 0.804 μN, shows that rolling is not the first motion mode.

6.3 Effect of Material Stiffness: Case B (E = 102.87 GPa, G = 40.5 GPa)

For case B, E = 102.87 GPa and G = 40.5 GPa. These values are mutually consistent: for an isotropic material G = E/[2(1+ν)], so ν = E/(2G) − 1 = 0.270, a typical value for silicon-based materials; case

C (E = 169 GPa, G = 66.54 GPa) gives the same ν = 0.270. In case B the pre-load and the lateral loading rate are F_Z = 0.50 μN and k_cV_{sub} = 3.25 μN/s (Table 3). The sliding threshold is reached at t* = 0.134 s with F* = 0.664 μN (Figure 10), and the rolling threshold at t = 0.200 s with F_{roll} = 0.821 μN (Figure 11); F_{roll}/F_{slide} = 1.24. Compared with the baseline case, the critical force changes by only 2.6 % because F^*_s is set by F_Z and A_{sp} (a_{sp} = 20.4 nm), which hardly change, whereas the onset time is 37 % shorter because the lateral force is applied 63 % faster. The poles of F^*_s and F^*_r move to 0.123 s and 0.089 s. Table 3 summarises the three material cases.

Table 3. The three cases: pre-load F_Z, lateral loading rate k_cV_{sub} (JKR contact radius a_{sp}, and the resulting onset conditions. ν = E/(2G) − 1 = 0.270 for cases B and C.

Case	F_Z (μN)	k_cV_{sub} (μN/s)	a_{sp} (nm)	Sliding: t*, F*	Rolling: t, F_{roll}	F_{roll}/F_{slide}
A (baseline; E = 102.87 GPa, G = 40.5 GPa)	0.487	2.00	20.3	0.213 s, 0.647 μN	0.320 s, 0.804 μN	1.24
B (E = 102.87, G = 40.5 GPa)	0.50	3.25	20.4	0.134 s, 0.664 μN	0.200 s, 0.821 μN	1.24
C (E = 169, G = 66.54 GPa)	0.30	1.98	18.3	0.136 s, 0.403 μN	0.234 s, 0.551 μN	1.37

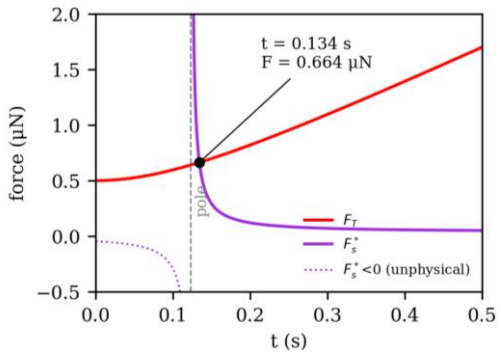


Figure 10. Tip force F_T and sliding critical force F^*_s for case B (E = 102.87 GPa, G = 40.5 GPa): sliding onset at t* = 0.134 s, F* = 0.664 μN.

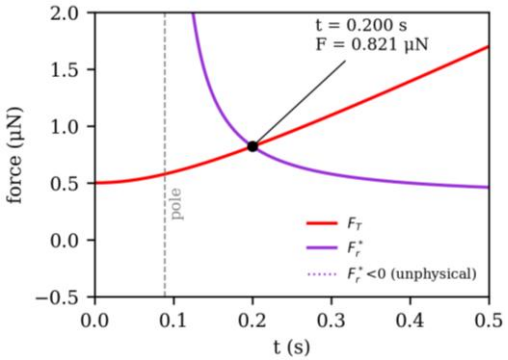


Figure 11. Tip force F_T and rolling critical force F^*_r for case B: intersection at t = 0.200 s, F_{roll} = 0.821 μN.

6.4 Effect of Material Stiffness: Case C (E = 169 GPa, G = 66.54 GPa)

For case C ($\nu = 0.270$) the pre-load is lower, $F_Z = 0.30$ μN, with $k_c V_{sub} = 1.98$ μN/s. The sliding threshold is reached at $t^* = 0.136$ s with $F^* = 0.403$ μN, and the rolling threshold at $t = 0.234$ s with $F_{roll} = 0.551$ μN (Figures 12 and 13); $F_{roll}/F_{slide} = 1.37$. The lower pre-load reduces both the load term $\mu_s F_Z$ and the contact radius ($a_{sp} = 18.3$ nm), so the critical sliding force is 38 % lower than in the baseline case, and the margin between rolling and sliding is the largest of the three cases. Taken together, cases A–C show that the critical force is governed by the pre-load F_Z, and the onset time by the loading rate $k_c V_{sub}$. Because E and G are linked through ν for an isotropic material, cases B and C vary the two moduli together; the separate influence of E and of G cannot be isolated, and the two cases should be read as a joint stiffness scan.

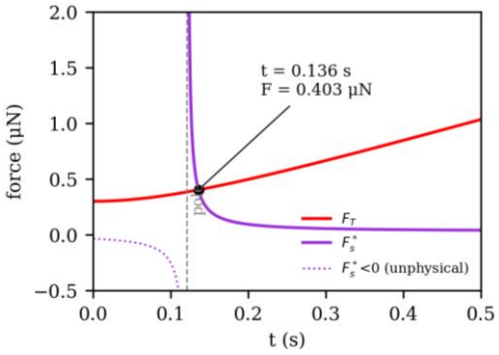


Figure 12. Tip force F_T and sliding critical force F^*_s for case C: sliding onset at $t^* = 0.136$ s, $F^* = 0.403$ μN.

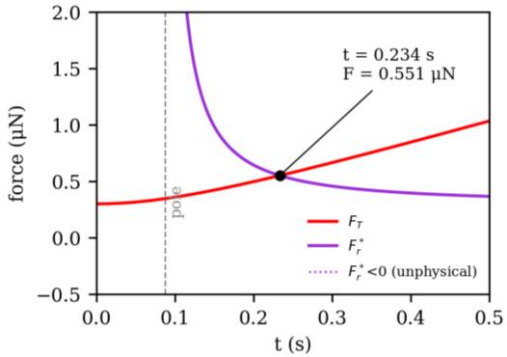


Figure 13. Tip force F_T and rolling critical force F^*_r for case C: intersection at $t = 0.234$ s, $F_{roll} = 0.551$ μN.

6.5 Phase II: Solution of Newton's Second Law

Figure 14 shows the force components of Phase I for the baseline case: the lateral force F_Y rises linearly at $k_c V_{sub} = 2.0$ μN/s to $F_s = 0.426$ μN at t^*, while the normal force $F_Z = 0.487$ μN is constant, so that F_T reaches 0.647 μN. The dashed lines are the constant forces that a quasi-static Phase II would keep after t^*. Figure 15 shows the solution of Eqs. (9)–(13) for the same loading, with $V_{sub} = 1$ μm/s, $k_c = 2.0$ N/m, $R_p = 500$ nm ($m = 1.0\times10^{-14}$ kg) and $\zeta = 0.886$.

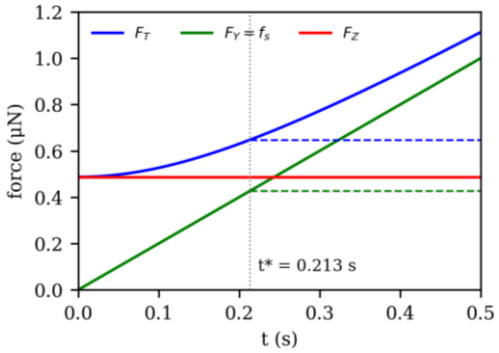


Figure 14. Force components in Phase I, baseline case: resultant tip force F_T, lateral force $F_Y = f_s$ and normal force F_Z; dashed lines: forces held constant after t* in a quasi-static Phase II (compare Fig. 15a).

The solution is a stick–slip cycle (Fig. 15a). At t* the particle slips backwards relative to the substrate under the stored elastic force. The slip lasts t_{slip} = 0.22 μs (Fig. 15b,c); the lateral force falls from F_s = 0.426 μN to $F_{min} = (2\zeta - 1)F_s$ = 0.329 μN; the particle moves $2(1 - \zeta)F_s/k_c$ = 49 nm relative to the substrate, with a peak relative speed of 0.34 m/s; and it then sticks again. The force is reloaded at the rate $k_c V_{sub}$ during t_{stick} = 49 ms, and the cycle repeats at about 20 Hz. The mean velocity of the particle relative to the substrate is the substrate velocity, which was the result of a quasi-static Phase II; the two models therefore agree in the mean motion but differ in the force history, a saw-tooth instead of a constant.

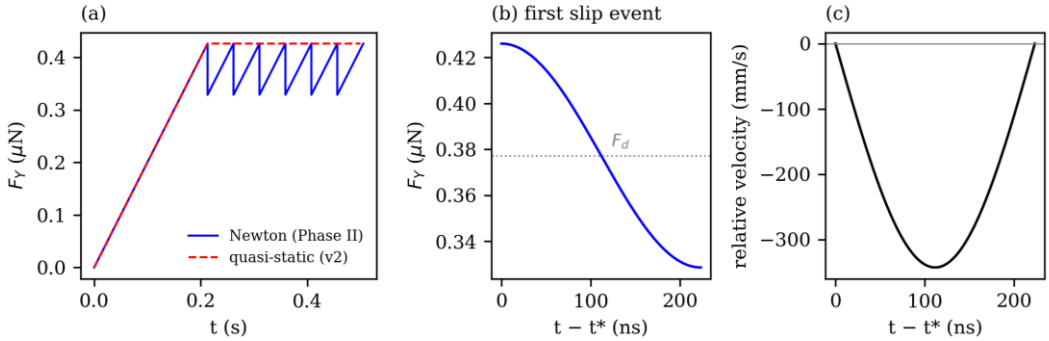


Figure 15. Phase II from Newton's second law (Eqs. 9–13), baseline parameters: (a) lateral force F_Y versus time, compared with the constant-force quasi-static assumption; (b) first slip event on a nanosecond scale (dotted line: kinetic friction force F_d); (c) velocity of the particle relative to the substrate during the same event.

Inertia enters only through the slip duration. Because $t_{slip} \propto \sqrt{m}$, increasing R_p from 20 nm to 5 μm lengthens the slip from 1.8 ns to 7.1 μs while F_{min} is unchanged (Fig. 19c). Adding the modal mass of the cantilever ($m_{eff} \sim 10^{-12}$ kg) raises t_{slip} to about 2.2 μs, and ε stays below 10^{-5}. Viscous damping with damping ratios $c/(2\sqrt{(k_c m)})$ of 0.05, 0.2 and 0.5 raises F_{min} from 0.329 μN to 0.336, 0.352 and 0.369 μN and lengthens the slip by at most 15 %. The friction ratio ζ is the controlling parameter: from ζ = 0.875 to 0.99, F_{min} rises from 0.320 to 0.417 μN and the stick period falls from 53 ms to 4.3 ms; area-dominated friction ($\zeta \to 1$) removes the stick–slip cycle.

6.6 Dynamic Instabilities: Stick–Slip and Snap-Through

Stick–slip is the instability captured by the present model. It arises because the kinetic friction force is lower than the static one ($\zeta < 1$) and the cantilever is compliant, and it is the counterpart of the atomic stick–slip observed in friction force microscopy [29-30]. The slip length $2(1 - \zeta)F_s/k_c$ = 49

nm and the period $2(1-\zeta)F_s/(k_cV_{sub}) = 49$ ms are testable predictions (Eq. 13); a stiffer cantilever or a faster substrate shortens both. The lateral force in the cycle never exceeds F_s, so the rolling threshold is not reached. Velocity-dependent friction [30] and LuGre-type pre-sliding [35] would soften the abrupt force drop and are not included.

Snap-through is not captured, because the tip is kept in contact by the pre-displacement δ_0. Jump-in or snap-off of the tip–particle contact occurs when the gradient of the adhesive force exceeds the cantilever stiffness, $|\partial F_{adh}/\partial z|_{max} > k_c$ [32]; for JKR contacts it is accompanied by adhesion hysteresis between loading and unloading [27,31]. It is relevant to the approach and release stages of a manipulation cycle and would require the tip–particle gap to be a dynamic variable. It is listed as a limitation in Section 7.

6.7 Parametric Sensitivity Analysis

Figures 16–18 show the forces at which sliding ($F_T = F^*_s$) and rolling ($F_T = F^*_r$) start as functions of the particle radius, the tip radius and the contact angle, giving guidelines for experimental protocol design.

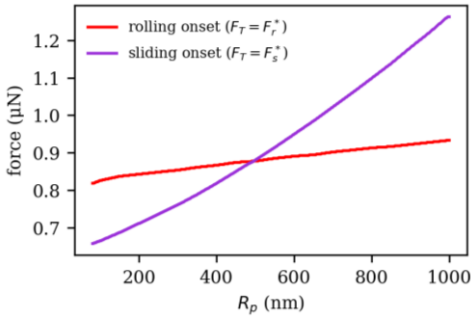


Figure 16. Forces at the onset of sliding and of rolling versus nanoparticle radius R_p. The sliding force increases faster with R_p than the rolling force, because the contact area and hence τA_{sp} grow with R_p; the two curves approach each other near $R_p \approx 0.5$ μm.

With increasing R_p the sliding threshold rises from 0.66 μN at 80 nm to 1.26 μN at 1 μm, and the rolling threshold from 0.82 to 0.93 μN (Fig. 16): the margin between the two modes shrinks with particle size, and near $R_p \approx 0.5$ μm the two thresholds approach each other, which indicates the particle size at which the sliding-before-rolling ordering is expected to reverse. In contrast, the sliding threshold is constant, 0.647 μN, over the whole range of tip radius (12–50 nm, Fig. 17) and contact angle (0.05–1.3 rad, Fig. 18), as Eq. (6) predicts, while the rolling threshold increases from 0.81 to 0.87 μN with the tip radius (20–50 nm) and from 0.69 to 0.89 μN with the contact angle (0.2–1.3 rad). The sliding-before-rolling ordering therefore holds over the whole range of R_{tip} and α studied, and the contact angle is the most effective parameter for widening the margin.

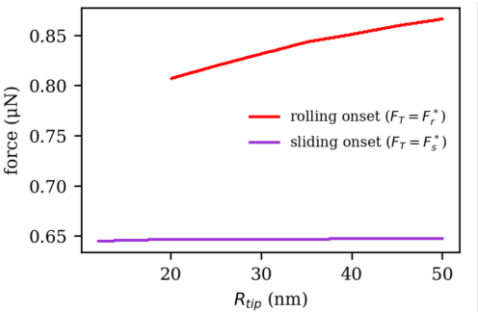


Figure 17. Forces at the onset of sliding and of rolling versus probe tip radius R_{tip}: the sliding force is independent of R_{tip} and the rolling force increases with it.

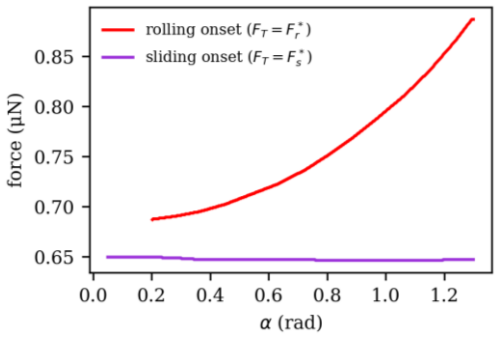


Figure 18. Forces at the onset of sliding and of rolling versus the tip–particle contact angle α: the sliding force is independent of α, and the rolling force increases with α.

6.8 Verification and Validation

Four quantities are calibrated: the work of adhesion w = 21.4 mJ/m², chosen so that the JKR model gives a_{sp} = 20.3 nm (Fig. 6); the rolling-resistance coefficient κ = 14.8, fitted to the rolling onsets of the three cases; and, for each case, the pair (F_Z, $k_c V_{sub}$) of Table 3, which is set by the pre-displacement and the cantilever. Given these, the sliding onset follows from Eq. (6) without further adjustment. Because the rolling coefficient is fitted, the rolling thresholds are consistency checks and not predictions.

A slip event has the closed-form solution of Eq. (12). Figure 19a shows the relative error of the minimum force F_{min} obtained with a fixed-step fourth-order Runge–Kutta scheme as the step $\Delta\eta = \omega\Delta t$ is reduced from 0.2 to 0.0125: the error falls from 6.1×10^{-4} to 2.6×10^{-6}, at second order, which is the order of the linear interpolation used to locate the event. The adaptive Dormand–Prince integrator with Max Step Size $0.05/\omega$ reproduces Eq. (12) with a relative error below 5×10^{-11} for tolerances between 10^{-5} and 10^{-11} (Fig. 19b), and t_{slip} and t_{stick} agree with the analytical values to better than 10^{-9}.

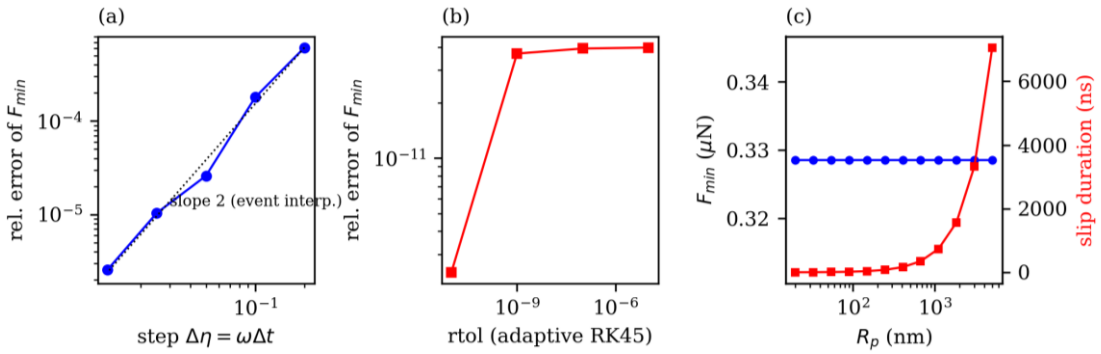


Figure 19. Verification of the integrator: (a) relative error of F_{min} versus step size for fixed-step RK4; (b) relative error versus tolerance for the adaptive Dormand–Prince integrator; (c) F_{min} (left axis) and slip duration (right axis) versus particle radius R_p.

The predicted critical sliding and rolling forces and their ratio are compared with the experimental results of [8] in Table 4. The deviation is quantified by the relative error $\varepsilon_F = |F_{model} - F_{exp}|/F_{exp}$ and, where the experimental curve is available at n points, by the normalised root-mean-square error

$$\mathrm{NRMSE} = [(1/n)\,\Sigma\,(F_{\mathrm{model},i} - F_{\mathrm{exp},i})^2]^{1/2}/(F_{\mathrm{exp,max}} - F_{\mathrm{exp,min}}).$$

Table 4. Comparison of the present model with the experimental results of [8]

Quantity	Present model	Sitti & Hashimoto [8]	Relative error ε_F
Critical sliding force F*	0.647 μN	0.61 μN	6.0%
Critical rolling force F_{roll}	0.804 μN	0.86 μN	6.5%
Ratio F_{roll}/F_{slide}	1.24	1.41	12.0%
First motion mode	sliding	Sliding	—

7. Limitations and Future Work

The model has the following limitations: (i) single-asperity JKR contact on smooth surfaces; (ii) elastic, time-independent deformation; (iii) one-dimensional lateral dynamics with constant normal force and without rotational degrees of freedom (rotational inertia I_θ is neglected as the primary predicted motion mode across the operating regime is pure sliding, and the rotational dynamics reach quasi-equilibrium on a sub-nanosecond timescale); (iv) dry contact, without capillary or electrostatic forces; (v) a permanent tip–particle contact, so that snap-through (Section 6.6) is not modelled; (vi) a rolling-resistance moment represented by one calibrated coefficient κ.

Soft and polymeric particles show time-dependent contact area and dissipation. The linear viscoelastic contact formulation of [36] and the theory of viscoelastic adhesive contact of [37] can replace the elastic JKR radius of Eq. (3) by a hereditary-integral relation a(t), and [19] have already combined rough and viscoelastic contact models for the first phase of three-dimensional biomanipulation. In the present framework this adds one internal-variable equation per interface to Eq. (9) and a rate dependence to F_s and F_d, and therefore to ζ and the stick–slip cycle.

Multi-asperity contact models [38] and adhesion corrections for rough surfaces [39] show that roughness reduces the real contact area and the effective adhesion. Recent theories of rough-surface contact and friction [40-41], the contact-mechanics benchmark of [42] and the multiscale overview of [43] provide area–load relations that can replace Eq. (3), with the area-dependent friction term τA_{sp} evaluated for the real contact area. Both extensions modify a(N, t) in Eqs. (3)–(6) and leave Eq. (9) unchanged. Further extensions are tip–particle gap dynamics for snap-through, LuGre friction [35], cantilever dynamics [25] and closed-loop control [14].

8. Conclusions

This paper has presented a dynamic simulation of AFM-tip-driven manipulation of a spherical gold nanoparticle with JKR contact mechanics and a modified Coulomb friction law. The two-phase algorithm gives the onset time t* and the critical force F* in Phase I from explicit sliding and rolling thresholds; in Phase II the particle motion follows from Newton's second law, integrated with an adaptive Runge–Kutta scheme with event detection, which was verified against the analytical solution and a convergence study. The inertial time scale of the particle is about 3×10^{-7} of t*, so a quasi-static description of the mean motion is accurate. The dynamic solution additionally predicts a stick–slip cycle between F_s and $(2\zeta - 1)F_s$ (0.43 to 0.33 μN for ζ = 0.89), with 49 nm slip events of about 0.2 μs repeated at about 20 Hz. Sliding precedes rolling in all cases (F_{roll}/F_{slide} = 1.24 to

1.37), consistent with literature, and the rolling threshold is not reached during stick–slip. The sliding threshold is independent of tip radius and contact angle, whereas the rolling threshold increases with both; the ordering is expected to reverse for particles near 0.5 μm in radius. The critical force is governed by the normal pre-load (0.647 μN at F_Z = 0.487 μN; 0.403 μN at 0.30 μN), and the onset time by the lateral loading rate (0.213 s at 2.0 μN/s; 0.134 s at 3.25 μN/s). Because E and G are linked through ν = 0.270, they are varied jointly. The critical force F* increases with the nanoparticle radius R_p; the rolling force increases with R_{tip} and α, so precise tip positioning matters. Viscoelasticity, surface roughness, snap-through and environmental effects are the main extensions.

References

[1] Binnig, G., Rohrer, H., Gerber, Ch., & Weibel, E. (1982). Surface studies by scanning tunneling microscopy. *Physical Review Letters, 49(1),* 57–61. https://doi.org/10.1103/PhysRevLett.49.57.

[2] Binnig, G., Quate, C. F., & Gerber, Ch. (1986). Atomic force microscope. *Physical Review Letters, 56(9),* 930–933. https://doi.org/10.1103/PhysRevLett.56.930.

[3] Eigler, D. M., & Schweizer, E. K. (1990). Positioning single atoms with a scanning tunnelling microscope. *Nature, 344(6266),* 524–526. https://doi.org/10.1038/344524a0.

[4] Binnig, G., & Rohrer, H. (1987). Scanning tunneling microscopy — from birth to adolescence. *Reviews of Modern Physics, 59(3),* 615–625. https://doi.org/10.1103/RevModPhys.59.615.

[5] Crommie, M. F., Lutz, C. P., & Eigler, D. M. (1993). Confinement of electrons to quantum corrals on a metal surface. *Science, 262(5131),* 218–220. https://doi.org/10.1126/science.262.5131.218.

[6] Dong, L. X., Arai, F., & Fukuda, T. (2002). Three-dimensional nanorobotic manipulations of carbon nanotubes. *Journal of Robotics and Mechatronics (JSME), 14(3),* 245–252.

[7] Fukuda, T., Arai, F., & Dong, L. X. (2003). Assembly of nanodevices with carbon nanotubes through nanorobotic manipulations. *Proceedings of the IEEE, 91(11),* 1803–1818. https://doi.org/10.1109/JPROC.2003.818334.

[8] Sitti, M., & Hashimoto, H. (2000). Controlled pushing of nanoparticles: Modeling and experiments. IEEE/ASME Transactions on Mechatronics, 5(2), 199–211. https://doi.org/10.1109/3516.847093.

[9] Sitti, M., Aruk, B., Shintani, K., & Hashimoto, H. (2003). *Scaled teleoperation system for nanoscale interaction and manipulation. Advanced Robotics, 17(3),* 275–291. https://doi.org/10.1163/156855303764018446.

[10] Korayem, M. H., & Zakeri, M. (2009). Sensitivity analysis of nanoparticles pushing critical conditions in 2-D controlled nanomanipulation based on AFM. *International Journal of Advanced Manufacturing Technology, 41(7–8),* 714–726. https://doi.org/10.1007/s00170-008-1519-0.

[11] Korayem, M. H., & Taheri, M. (2014). Modeling of various contact theories for the manipulation of different biological micro/nanoparticles based on AFM. *Journal of Nanoparticle Research, 16(4),* 2321. https://doi.org/10.1007/s11051-014-2321-9.

[12] Korayem, M. H., Saraee, M. B., Mahmoodi, Z., & Dehghani, S. (2015). Modeling and simulation of three-dimensional manipulations of biological micro/nanoparticles by applying cylindrical contact mechanics models by means of AFM. *Journal of Nanoparticle Research, 17(11),* 439. https://doi.org/10.1007/s11051-015-3240-x.

[13] Korayem, M. H. (2021). Dynamic modeling of a cylindrical nanoparticle manipulation by AFM. *Engineering Science and Technology, an International Journal, 24(3),* 714–727. https://doi.org/10.1016/j.jestch.2020.12.003.

[14] Korayem, M. H., & Omidi, E. (2012). Robust controlled manipulation of nanoparticles using atomic force microscope. *IET Micro & Nano Letters, 7(9*), 927–932. https://doi.org/10.1049/mnl.2012.0375.

[15] Requicha, A. A. G. (2003). Nanorobots, NEMS, and nanoassembly. *Proceedings of the IEEE, 91(11),* 1922–1933. https://doi.org/10.1109/JPROC.2003.818333.

[16] Johnson, K. L., Kendall, K., & Roberts, A. D. (1971). Surface energy and the contact of elastic solids. *Proceedings of the Royal Society of London A, 324(1558),* 301–313. https://doi.org/10.1098/rspa.1971.0141.

[17] Derjaguin, B. V., Muller, V. M., & Toporov, Yu. P. (1975). Effect of contact deformations on the adhesion of particles. *Journal of Colloid and Interface Science, 53(2*), 314–326. https://doi.org/10.1016/0021-9797(75)90018-1.

[18] Ando, T., Uchihashi, T., & Fukuma, T. (2008). High-speed atomic force microscopy for nano-visualization of dynamic biomolecular processes. *Progress in Surface Science, 83(7–9),* 337–437. https://doi.org/10.1016/j.progsurf.2008.09.001.

[19] Korayem, M. H., Mozafari, M., Sooha, Y. H., & Rastegar, Z. (2021). Development and application of rough viscoelastic contact models in the first phase of 3D manipulation for biological micro-/nanoparticles by AFM. *Archive of Applied Mechanics, 91(9),* 3739–3753. https://doi.org/10.1007/s00419-021-01967-5.

[20] Degertekin, F. L., et al. (2006). Nanoscale imaging with FIRAT: A force sensing integrated readout and active tip. *Review of Scientific Instruments, 77(2),* 023701. https://doi.org/10.1063/1.2167130.

[21] Ma, X.; Wang, W.; Xie, G.; Guo, D.; Wen, S. (2020). Friction measurement and motion state determination of a single polystyrene nanoparticle during manipulation. *Micro Nano Lett. , 15,* 1140–1145.

[22] Kim, H. J., Kang, K. H., & Kim, D. E. (2013). Sliding and rolling frictional behavior of a single ZnO nanowire during manipulation with an AFM. *Nanoscale, 5(13),* 6081–6087. https://doi.org/10.1039/c3nr01433e.

[23] Hou, L., Hou, M., Yibibulla, T. *et al.* (2022). Frictional shear stress of ZnO nanowires on natural and pyrolytic graphite substrates. Friction 10, 2059–2068. https://doi.org/10.1007/s40544-021-0577-2.

[24] Dong, L. X., Arai, F., & Fukuda, T. (2004). Destructive constructions of nanostructures with carbon nanotubes through nanorobotic manipulation. *IEEE/ASME Transactions on Mechatronics, 9(2),* 350–357. https://doi.org/10.1109/TMECH.2004.828671.

[25] Wuweikai Xiang, Yanling Tian, Xianping Liu. (2020). Dynamic analysis of tapping mode atomic force microscope (AFM) for critical dimension measurement, *Precision Engineering, Volume 64,* Pages 269-279, https://doi.org/10.1016/j.precisioneng.2020.03.023.

[26] Tafazzoli, A., & Sitti, M. (2004). Dynamic behavior and simulation of nanoparticle sliding during nanoprobe-based positioning. *ASME International Mechanical Engineering Congress and Exposition (IMECE 2004).*

[27] Maugis, D. (1992). Adhesion of spheres: the JKR-DMT transition using a Dugdale model. *Journal of Colloid and Interface Science, 150(1),* 243–269.

[28] Savkoor, A. R., & Briggs, G. A. D. (1977). The effect of tangential force on the contact of elastic solids in adhesion. *Proceedings of the Royal Society of London A, 356,* 103–114.

[29] Carpick, R. W., & Salmeron, M. (1997). Scratching the surface: fundamental investigations of tribology with atomic force microscopy. *Chemical Reviews, 97(4),* 1163–1194.

[30] Gnecco, E., Bennewitz, R., Gyalog, T., Loppacher, Ch., Bammerlin, M., Meyer, E., & Güntherodt, H.-J. (2000). Velocity dependence of atomic friction. *Physical Review Letters, 84(6),* 1172–1175.

[31] Tabor, D. (1977). Surface forces and surface interactions. *Journal of Colloid and Interface Science, 58(1),* 2–13.

[32] Cappella, B., & Dietler, G. (1999). Force-distance curves by atomic force microscopy. *Surface Science Reports, 34(1–3),* 1–104.

[33] Hairer, E., Nørsett, S. P., & Wanner, G. (1993). Solving Ordinary Differential Equations I: Nonstiff Problems (2nd ed.). Springer.

[34] Dormand, J. R., & Prince, P. J. (1980). A family of embedded Runge–Kutta formulae. *Journal of Computational and Applied Mathematics, 6(1),* 19–26.

[35] Canudas de Wit, C., Olsson, H., Åström, K. J., & Lischinsky, P. (1995). A new model for control of systems with friction. *IEEE Transactions on Automatic Control, 40(3),* 419–425.

[36] Lee, E. H., & Radok, J. R. M. (1960). The contact problem for viscoelastic bodies. *Journal of Applied Mechanics, 27(3),* 438–444.

[37] Greenwood, J. A., & Johnson, K. L. (1981). The mechanics of adhesion of viscoelastic solids. *Philosophical Magazine A, 43(3),* 697–711.

[38] Greenwood, J. A., & Williamson, J. B. P. (1966). Contact of nominally flat surfaces. *Proceedings of the Royal Society of London A, 295,* 300–319.

[39] Fuller, K. N. G., & Tabor, D. (1975). The effect of surface roughness on the adhesion of elastic solids. *Proceedings of the Royal Society of London A, 345*, 327–342.

[40] Persson, B. N. J. (2001). Theory of rubber friction and contact mechanics. *Journal of Chemical Physics, 115(8),* 3840–3861.

[41] Pastewka, L., & Robbins, M. O. (2014). Contact between rough surfaces and a criterion for macroscopic adhesion. *Proceedings of the National Academy of Sciences, 111(9),* 3298–3303.

[42] Müser, M. H., Dapp, W. B., Bugnicourt, R., et al. (2017). Meeting the contact-mechanics challenge. *Tribology Letters, 65*, 118.
[43] Vakis, A. I., Yastrebov, V. A., Scheibert, J., et al. (2018). Modeling and simulation in tribology across scales: an overview. *Tribology International, 125*, 169–199.